Paper ID: ETC2019-158
Proceedings of 13th European Conference on Turbomachinery Fluid dynamics & Thermodynamics ETC13, April 8-12, 2019; Lausanne, Switzerland

COUPLED FE-CFD ANALYSIS OF TRANSIENT CONJUGATE HEAT TRANSFER

A. P. Schindler - S. Brack - J. von Wolfersdorf

Institute of Aerospace Thermodynamics, University of Stuttgart, Stuttgart, Germany,
alexander.schindler@itlr.uni-stuttgart.de

ABSTRACT

Steady and transient conjugate heat transfer is examined using an efficient approach to couple a finite element code with a computational fluid dynamics solver. A combination of Dirichlet and Robin conditions was used to exchange data at the interface between adjacent solid and fluid domains. Among the computational aspects considered are appropriate coupling coefficients for the Robin condition, the coupling's convergence behavior and stability limits as well as the accuracy of the solution. Starting from a steady state coupling, transient solid calculations were coupled with a sequence of steady fluid solutions. Of particular interest was the extension of findings from a validation case with two-dimensional flow to a more complex one with flow around a three-dimensional vortex generator. The results obtained with the coupling method show good agreement with conjugate reference calculations and transient experiments that examined the spatio-temporal surface temperature using infrared thermography.

KEYWORDS

transient, conjugate, heat transfer, coupling, FEA, CFD

NOMENCLATURE

c_p	specific heat in $\mathrm{J\,kg^{-1}\,K^{-1}}$	ν	subiteration number
h	coupling coefficient in $\mathrm{W\,m^{-2}\,K^{-1}}$	ρ	density
i, m	indices	$\mathbf{\Phi}$	vector
n	wall-normal distance in m	CFD	computational fluid dynamics
k	thermal conductivity in $\mathrm{W\,m^{-1}\,K^{-1}}$	CHT	conjugate heat transfer
p	pressure in Pa	cpl	coupling
$\mathrm{Pr_t}$	turbulent Prandtl number	f	fluid
q	wall heat flux in $\mathrm{W\,m^{-2}}$	FE(A)	finite element (analysis)
t	time in s	FV	finite volume
T	temperature in K	I	interface
U	streamwise velocity in $\mathrm{m\,s^{-1}}$	nw	near-wall
u_τ	friction velocity in $\mathrm{m\,s^{-1}}$	rbf	radial basis function
x, y, z	coordinates in m	ref	reference
α	coupling coefficient	rms	root mean square
ε	norm	s	solid
η	dynamic viscosity in $\mathrm{Pa\,s}$	VG	vortex generator

INTRODUCTION

Thermal processes in aero engines are characterized by conjugate interactions of solid structure and fluid flow as well as transient behavior due to dynamic operation. The different operat-

ing points are considered in the design by analyzing generic or critical steady load cases. Sun et al. (2012) emphasized the relevance of examining the transient change between operating points that results in a variation of clearances and thermal stresses caused by inhomogeneous heating or cooling. Convective heat transfer in the fluid is often substantially faster than the solid heat conduction. Consequently, a conjugate simulation of a complete mission considering all time scales is prohibitively expensive. Methods to address this disparity of time scales are of major interest (see Sun et al., 2010; Errera and Baqué, 2013). The solid's thermal behavior is preferably calculated by finite element (FE) codes. Modeling the adjacent flow by means of Computational Fluid Dynamics (CFD) improves the thermal analysis. In order to ensure a physical solution of the conjugate system, the separate codes need to be coupled at their common interface. Several free (Bungartz et al., 2016; Duchaine et al., 2015) and commercial (Joppich and Kuerschner, 2006) programs provide coupling solutions for multiphysics. Some studies, such as Gimenez et al. (2016), discuss the methodology mainly with respect to mathematical-numerical aspects, while the demonstration is restricted to simple applications like a flat plate boundary layer. Others examined complex turbine cavities during real flight cycles (Sun et al., 2010), but reveal few details on how the coupling settings and parameters affect the solution. It is often not clearly described how experimental and computational reference data were obtained.

We present an approach to efficiently model transient conjugate heat transfer during operating point changes by coupling two existing codes. A modular Python-based coupling environment has been developed in-house, which allows to examine various coupling methods in one framework and therefore a distinct analysis of functionalities and their interaction, while employing free and open-source software only. The aim of this paper is to verify and evaluate two different coupling concepts, reveal their characteristics, and provide a numerical method to complement transient, conjugate heat transfer experiments. For this purpose, two test cases have been chosen: Flow and conjugate heat transfer in a channel with a flat plate in its center are examined in order to validate the coupling environment and derive appropriate coupling settings for steady and transient applications. Subsequently, the findings are transferred to the more complex setup with flow around a three-dimensional vortex generator (VG). Similarities and differences of the coupling setup are discussed and results of transient experiments are shown for comparison. Additionally, we address in detail the coupling method with regard to computational effort and alternative approaches.

NUMERICAL METHODOLOGY

The conjugate problem comprises two adjacent regions: a solid and a fluid subdomain that share a mutual interface. Heat conduction in the solid subdomain was calculated using the open-source FE code CalculiX®. Although its capabilities cover a wide range of applications, a pure heat transfer analysis with linear eight-noded hexahedral elements was conducted for this paper. The flow modeling capabilities of the solver chtMultiRegionFoam of the open-source CFD code OpenFOAM® were applied to the adjacent fluid subdomain. Apart from a modification of the energy equation as a means to account for viscous dissipation, only original features were used. Dry air was modeled as perfect gas, assuming temperature-dependent fluid properties. The Shear Stress Transport turbulence model was applied without wall functions, therefore requiring a high near-wall mesh resolution of $\Delta n_1^+ = u_\tau \Delta n_1 \rho_\mathrm{f}/\eta_\mathrm{f} < 1$. The turbulent Prandtl number was set to $\mathrm{Pr_t} = 0.85$. Turning to details of the spatial finite volume (FV) discretization, second-order linear upwind schemes were used for all convective terms but the turbulent fluxes, which were approximated with first-order upwind interpolation. Diffusive terms were treated linearly.

The time derivative was omitted for the steady CFD calculations.

The temperature T and the specific heat flux q on both sides of the common interface I are required to satisfy $T_{\mathrm{s,I}} = T_{\mathrm{f,I}}$ and $q_{\mathrm{s,I}} = q_{\mathrm{f,I}}$ in order to yield a physical solution. For this purpose, a Python-based coupling environment has been developed to manage the information exchange at the interface. Data inter- and extrapolation at the interface from one domain to the other is needed because the adjacent meshes are not necessarily congruent. The SciPy package (see Jones et al., 2001) offers a variety of options for three-dimensional scattered data mapping from which we used a linear multivariate griddata interpolation (default) and linear radial basis functions (rbf). With regard to the efficient modeling of long missions, it proved beneficial to perform a transient FE analysis (FEA) that yields the spatio-temporal temperature evolution in the structure. At selected times t_i, a steady CFD calculation is performed, enabling a thermal feedback and interface update. The sequential coupling algorithm works as follows. Starting from a converged solution at t_{i-1}, the transient FEA advances from t_{i-1} to t_i by a coupling interval Δt_{cpl}. In the course of this, a Robin condition

$$q^{\nu}_{\mathrm{s,I}}(t) = h^{\nu}(t)(T^{\nu}_{\mathrm{s,I}}(t) - T^{\nu}_{\mathrm{ref}}(t)) \tag{1}$$

is imposed on the solid side interface as recommended by Errera et al. (2017) for small Biot numbers. The superscript $\nu = \{1, 2, 3, ..., \nu_{\max}\}$ denotes the current subiteration. The first subiteration $\nu = 1$ of this coupling step uses constant h^{ν} and T^{ν}_{ref} based on t_{i-1}. Subsequently, the FEA results at t_i are imposed as a Dirichlet condition on the fluid side for the steady CFD:

$$T^{\nu}_{\mathrm{f,I}}(t_i) = T^{\nu}_{\mathrm{s,I}}(t_i) \tag{2}$$

This steady CFD yields fluid results from which $T^{\nu+1}_{\mathrm{ref}}(t_i)$ and $h^{\nu+1}(t_i)$ will be derived. Now, the next subiteration $\nu + 1$ of the same coupling step from t_{i-1} to t_i starts. The new $h^{\nu+1}(t)$ and $T^{\nu+1}_{\mathrm{ref}}(t)$ are linearly ramped from the converged values of the old coupling step at t_{i-1} to $T^{\nu+1}_{\mathrm{ref}}(t_i)$ and $h^{\nu+1}(t_i)$ that have been derived from the CFD results of the previous subiteration ν. The FEA advances again from t_{i-1} to t_i with the updated, now transient Robin condition (1) and yields a new $T^{\nu+1}_{\mathrm{s,I}}(t_i)$ that is imposed on the subsequent steady CFD. This sequence of subiterations during one coupling step is repeated until interfacial convergence and therefore a time-accurate solution at t_i is reached. Before proceeding with the next coupling step from t_i to t_{i+1}, convergence is checked at the end of each subiteration by either the infinity norm

$$\varepsilon_{\infty} = \|\mathbf{\Phi}\|_{\infty} = \max_{m} |\Phi_m| < \varepsilon_{\max} \tag{3}$$

as used by Errera et al. (2017) or a root mean square (rms) evaluation

$$\varepsilon_{\mathrm{rms}} = \left(M^{-1} \sum_{m=1}^{M} (\Phi_m^2) \right)^{0.5} < \varepsilon_{\max} \tag{4}$$

where Φ_m depends on the exchanged variables. In the results presented here, $\Phi_m = T^{\nu}_{\mathrm{f,I},m} - T^{\nu-1}_{\mathrm{f,I},m}$ where m is one of all M points on the interface.

Concerning appropriate choices for h and T_{ref}, we examined the following two options.

$$\text{Option 1} = \begin{cases} h^{\nu}(t_i) = h = \text{constant} \\ T^{\nu}_{\mathrm{ref}}(t_i) = \frac{-q^{\nu-1}_{\mathrm{f,I}}(t_i)}{h} + T^{\nu-1}_{\mathrm{f,I}}(t_i) \end{cases} \tag{5}$$

The relaxation parameter h in equation (5) is globally defined (cf. Errera et al., 2017) and T_{ref} is based on the local fluid-sided interface values $q^{\nu-1}_{\mathrm{f,I}}$ and $T^{\nu-1}_{\mathrm{f,I}}$ of the previous subiteration. For convenience, the non-dimensional parameter $\alpha = h/(1\ \mathrm{W\,m^{-2}\,K})$ is introduced. It will be shown that varying the values for α affects the coupling convergence and stability significantly.

Turning now to a locally varying parameter, the definition reads

$$\text{Option 2} = \begin{cases} h^{\nu}(t_i) = \left| \frac{q_{\mathrm{f,I}}^{\nu-1}(t_i)}{T_{\mathrm{f,I}}^{\nu-1}(t_i) - T_{\mathrm{f,nw}}^{\nu-1}(t_i)} \right| \\ T_{\mathrm{ref}}^{\nu}(t_i) = T_{\mathrm{f,nw}}^{\nu-1}(t_i) \end{cases} \tag{6}$$

where $T_{\mathrm{f,nw}}^{\nu-1}$ is the near-wall fluid temperature at a specified distance Δn from the interface. Option 2 was derived from Errera and Baqué (2013) who used the fluid temperatures of the first wall-adjacent cell, but noticed slow convergence. For the present study, the approach was modified so as to allow arbitrary Δn in order to examine the influence of the reference distance and possibly accelerate the convergence. Moreover, h^{ν} was artificially limited to $10^{-6}\ \mathrm{W\,m^{-2}\,K} < h^{\nu} < 10^{6}\ \mathrm{W\,m^{-2}\,K}$ in avoidance of vanishing convergence on the one hand and instability or rounding errors on the other hand. Note that Option 2 needs information from the internal CFD field, not only from the interface. Considering equations (1) and (2), $T_{\mathrm{f,I}}^{\nu} = T_{\mathrm{f,I}}^{\nu-1} = T_{\mathrm{s,I}}^{\nu} = T_{\mathrm{s,I}}^{\nu-1}$ yields $q_{\mathrm{s,I}}^{\nu} = q_{\mathrm{s,I}}^{\nu-1} = q_{\mathrm{f,I}}^{\nu} = q_{\mathrm{f,I}}^{\nu-1}$ for both options in case of convergence at t_i.

Results of the reference calculations have been obtained by employing the solver chtMultiRegionFoam in a different way as it also allows to calculate multiple physical domains inherently using the FV method in both regions. The subdomains were sequentially updated, while the interface temperatures were reconstructed by weighting the wall-closest cell center temperatures on both sides with a thermal conductance fraction. An Euler scheme was used for time integration of the transient reference calculations. All other modeling settings were the same as described above. Thus, the fluid treatment of the internal conjugate heat transfer (CHT) reference calculation is identical to the coupled FE-CFD analysis with externally connected codes.

Solving the full set of fluid equations is computationally expensive. One way to speed up the calculation is to freeze the steady flow field and solve the energy transport only, which omits temperature-induced changes in the flow field and is thus only applicable when the temperature differences are small. The sequence of steady CFD is accelerated because less equations are solved in one iteration. The transient reference CHT calculation is additionally accelerated as larger time steps can be utilized without negatively affecting stability. All transient reference calculations in this paper are based on a frozen flow. The full set of equations was solved for the coupled calculations where not otherwise stated.

TWO-DIMENSIONAL CHANNEL FLOW

Before discussing the VG's complex flow and heat transfer, we consider a two-dimensional conjugate channel flow in order to find suitable coupling settings.

Numerical Setup

The computational domain of the symmetric channel is depicted in figure 1. A Perspex plate with elliptical leading and tailing edges was mounted in its center. Flow entered the fluid domain at the inlet where a temporal inlet temperature variation as depicted in figure 2 was imposed, while the velocity $U_{\mathrm{inlet}} = 22.1\ \mathrm{m\,s^{-1}}$ was constant. The outlet pressure was $p_{\mathrm{outlet}} = 90204$ Pa and the top and bottom of the channel were no-slip walls. Only the upper part ($y > 0$ m) of the symmetric channel was modeled. The two-dimensional mesh was created in a block-structured way with one cell in the third dimension and solely hexahedral elements in both domains. Even though the element faces of the two regions were congruent at the common interface, interpolation was still necessary from the FE nodes to the FV face centers. The wall-

normal resolution was similar on both sides and met the requirement $\Delta n_1^+ < 1$ with an offset between the wall-adjacent cell centers and the interface of approximately $\Delta n_1 = 10^{-5}$ m.

Coupled Steady State

A converged CFD calculation with isothermal walls at $T_{\mathrm{f,I}} = T_{\mathrm{inlet}}(t = 0\ \mathrm{s})$ served as initialization of the coupled approach. The temperature in the solid FE domain was $T_s = T_{\mathrm{s,I}} = T_{\mathrm{inlet}}(t = 0\ \mathrm{s})$. Based on this initialization a coupled steady state was calculated. The local temperature variation at the interface was small and solely contributed to stagnation effects and viscous heating. The small variations turned out to be suitable for evaluating the coupling method's accuracy. The emphasis was on quickly obtaining an accurate temperature field at a converged steady state. So, temporal accuracy was subordinate and subiterations during one coupling step were superfluous. In terms of performance, it proved beneficial to run both the CFD and the FE code in a steady state mode, instead of letting transient calculations converge. Note that this procedure is only stable if appropriate relaxation, exchange and initial conditions are used. A fix number of 20 CFD solver iterations per coupling step was set. In the following, the choice of the coupling coefficients for the solid-side Robin condition is discussed. The global coefficient α, and thus h of equation (5), was varied from 100 to 5000, while T_{ref} was derived from the preceding interface values. Figure 3 (left) suggests that smaller α lead to faster convergence. However, the coupling diverges if α is smaller than a specific limit, which is between 100 and 200 in this case. While the trend is in line with results presented by Errera et al. (2017), apart from a non-monotonic behavior for small α, they obtained a stable solution for all $\alpha \geq 0$. Figure 4 illustrates the streamwise variation of interfacial temperature of the reference calculation besides the coupled results after 500 coupling steps. While good agreement can be observed for $\alpha = 200$, the deviation from the reference CHT calculation grows with larger α. Increasing the number of coupling steps does not improve the results since the convergence level is already negligible. Varying the distance Δn of the near-wall values of Option 2 in equation (6) also changes the convergence behavior. Smaller Δn result in slower convergence (cf. figure 3 (right)), but better accuracy. Overall, Option 1 with a global coupling coefficient α performs better with regard to convergence speed and the accuracy of the results. On the contrary, it can be challenging to choose an appropriate global α.

Transient Variation

Starting from the coupled steady state, we now turn to the transient calculation, where the unsteady FEA with fixed time increments $\Delta t_{\mathrm{FEA}} = 1$ s was coupled with a sequence of steady CFD with 1000 solver iterations. The logistic increase of the inlet temperature (cf. figure 2) was discretized in 5 s coupling intervals starting at 0 s. The initial steady flow field was frozen in order to focus on the temperature variation and allow comparison to the frozen reference CHT calculation. Temperature and wall heat flux on the Perspex plate surface at $t = 50$ s are plotted in figure 5. Both methods with $\alpha = 1000$ and $\Delta n =$ 1e-5 m predict slightly lower temperature values than the reference. The surface temperature evolution at $x = 0.402$ m is visualized in figure 6. In contrast to the steady state coupling, it is necessary to perform subiterations during each coupling step so as to predict the temporal behavior correctly. In order to emphasize the importance of convergence at each coupling step, the result of one calculation is added where the maximum number of subiterations was limited to $\nu \leq 3$. In this case, the error was propagated, whereas an adequate number of subiterations led to a minor maximal deviation of $\Delta T_{\mathrm{f,I}} = 0.15$ K at $t = 25$ s from the reference data. The bar graph in figure 6 represents the

required number of subiterations per coupling step to decrease $\varepsilon_{\mathrm{rms}} < 0.001$ K. The data suggest that the number of iterations correlates to the change of temperature between two successive coupling steps: The relatively large gradient from 20 to 25 s (cf. figure 2) demanded many subiterations during the corresponding fifth coupling step (cf. figure 6 (right)). Note that the number of subiterations per coupling step reduces when the coupling interval is chosen smaller. Moreover, the global $\alpha = 1000$ option converged faster than the variable near-wall approach, which confirms the findings from the coupled steady state calculations. In order to evaluate the frozen flow approach, we calculated the sequence of steady CFD with and without a frozen flow. The small temperature variation had only minor effects on the flow field and the maximum deviation of $\Delta T_{\mathrm{f,I}} = 0.24$ K occurred at $t = 55$ s and $x = 0.27$ m. The effect on performance was considerable though, with the frozen flow results being calculated 6 times faster.

THREE-DIMENSIONAL VORTEX GENERATOR FLOW

The following part of this paper moves on to extend the findings from the previously discussed two-dimensional channel to a three-dimensional vortex generator (VG). The induced eddy system strongly enhances the heat transfer in the obstacle's wake region and produces a distinct temperature footprint. Its characteristic qualifies for evaluating the coupling method. Comparison to the results of transient experiments complete the analysis. Both plate and VG are made from Perspex with $\rho_{\mathrm{s}} = 1190\ \mathrm{kg\,m^{-3}}$, $c_{p,\mathrm{s}} = 1470\ \mathrm{J\,kg^{-1}\,K^{-1}}$ and $k_{\mathrm{s}} = 0.19\ \mathrm{W\,m^{-1}\,K^{-1}}$.

Experimental Setup

Figure 7 shows a schematic of the experimental setup. A vacuum pump sucked ambient air through a dust filter. Two fine-wired mesh heaters that were connected to a power supply of 9.75 kW ensured a homogeneous temperature distribution of the air flow that entered the 0.12 m times 0.15 m test cross section. The VG was mounted on a 0.03 m thick plate with a distance of 0.29 m from its elliptical leading edge. A FLIR SC7600 infrared camera temporally and spatially resolved the surface temperature T_{I} in the VG's wake region with a frequency of 16 Hz. A black coating of the Perspex surface ensured a high emittance of the surface and a 5 mm thick CaF_2-window offered optical access. A type T Omega CO-2 surface thermocouple was applied to in situ calibrate the infrared thermography camera. During each experiment, the inlet fluid temperature T_{inlet} as well as the fluid velocity U_{inlet} could be controlled independently, using the mesh heater and the adjustable vanes downstream the test section. Two hot-wire probes at the inlet of the test section and fine-wire thermocouples measured the current T_{inlet} and U_{inlet}. In order to characterize the inlet flow conditions and deliver an accurate boundary condition for the numerical simulations, the inlet velocity profiles in y-direction have been measured beforehand. The induced surface heat flux $q_{\mathrm{I}}(x, z, t)$ was calculated by evaluating the T_{I}-measurements with the method according to Estorf (2006). Brack et al. (2018) give further details on the experimental setup, the evaluation method and the inlet velocity profiles.

Numerical Setup

The computational domain and the boundary conditions were derived from the experiments. Symmetry was utilized twice to reduce the computational effort. A comparative calculation with the full VG showed negligible influence of the symmetric boundary condition. Figure 8 shows a segment of the fluid domain. The streamlines illustrate the longitudinal vortex system that is induced by the VG and leads to a spatially varying heat transfer pattern in the wake region, which is described in detail by Henze et al. (2011). The hexahedral CFD grid exhibited a wall-

normal resolution of $\Delta n_1^+ < 1.25$ at the interface wall. This value increased to $\Delta n_1^+ < 3.2$ at the sharp edges of the VG. We performed calculations on grid resolutions from 0.7 over 1.6 up to 3.6 million cells covering the range examined by Dietz (2008). Oscillatory convergence, especially behind the VG, prevents the determination of a meaningful index. The medium resolution grid was used to demonstrate the coupling method, keeping possible grid dependence in mind. The FE grid was congruent at the common interface and particularly fine as a means to ensure that the features behind the VG do not become blurred.

Coupled Steady State

The initialization and isothermal steady pre-calculation were similar to the procedure described for the two-dimensional channel flow. Hence, the steady CFD and FE calculations were coupled without subiterations and the coupling coefficients were varied. The convergence is faster for smaller α as previously reported; however, the stability limit is shifted to a higher α between 500 and 1000. The points of the worst residual were located at the VG's sharp upper corner. This exemplifies the disadvantage of a global coupling coefficient when heat transfer and Δn_1^+ values vary spatially. On the contrary, the variable Δn approach also did not improve the convergence of this case and furthermore lacked accuracy.

In addition to the griddata interpolation, the linear rbf approach was utilized to perform the mapping from the FE nodes to the FV face centers. Convergence was only slightly affected, whereas the rbf interpolation error was larger. Moreover, the computational time for the coupling process (excluding both simulation runtimes) was 24 times higher than for the griddata interpolation and therefore unacceptable for a number of 22000 points.

Considering the total computational time of 10.7 hours for 200 coupling steps on 28 cores, the steady FE calculation required 64 %, the steady CFD with each 50 solver iterations 30 %, and the coupling process 6 %. Note that these values strongly depend on the separate simulation code settings such as the number of iterations, solver tolerances, and relaxation.

Transient Variation

Having obtained a coupled steady state, the temperature variation depicted in figure 2 was imposed on the inlet and a coupled solution was calculated. The unsteady FEA with $\Delta t_{\mathrm{FEA}} = 1$ s was coupled with a sequence of steady frozen CFD with 500 solver iterations each. The coupling interval and coefficient were $\Delta t_{\mathrm{cpl}} = 5$ s and $\alpha = 1000$. The contour plots in figure 10 illustrate the surface temperature distribution downstream of the VG at $t = 30$ s. Both numerical (left) and experimental (right) results share a number of key features such as the opening angle of the major vortex print, the existence of a secondary outer maximum at $x = 0.541$ m and $z = 0.037$ m, and a third maximum further downstream between the other two maxima. The computation predicts the major maxima to be less diffusive than the experiments suggest. This trend is also shown in figure 11 at a slice at $x = 0.54$ m. All considered calculations overshoot the experimental data in the region $|z| < 0.028$ m by ≈ 1 K which is associated with a higher absolute heat flux. The values for the secondary peaks as well as as for the minima at $|z| = 0.031$ m are comparable, though. Closer to the channel side walls the deviation increases again. The minor peak at $z = 0$ m is contributed to an increased wall shear stress in this region. It is also visible in the experimental data, but located further downstream and not as distinct. Good agreement with results from the reference calculation suggest that the deviation of the FE-CFD coupling from the experiments are not due to the coupling but rather caused by predicted differences in the flow field and heat transfer distribution. The maximum deviation of coupled

results and reference data in figure 11 is 0.26 K at $z = \pm 0.044$ m and the weighted arithmetic average is 0.07 K. These values are small considering that the sharp temperature extrema were resolved by a few cells only and that the reference calculation needed no interpolation from the FE nodes to the FV face centers. Considering the full set of fluid equations instead of a frozen flow field, shifts the results to slightly lower levels of temperature and absolute wall heat flux. Figure 9 shows that the good agreement at the interface point $x = 0.541$ m, $z = 0.037$ m is ensured for any time. The average of 15.1 subiterations was required to satisfy $\varepsilon_{\mathrm{rms}} < 0.001$ K. What stands out is that the final ε_{∞} (cf. equation 3) is 4 to 84 times larger than $\varepsilon_{\mathrm{rms}}$ with the maximum residual located at the VG's tip. In particular for complex flows, a slightly oscillating solution is not unusual even for a steady state CFD. Consequently, an rms norm may be the preferred residual calculation for such cases in order to deal with local oscillations. Apart from that, the coupling residual is no sufficient indicator for an accurate solution if the separate codes are not fully converged, particularly with regard to the temperature field.

Employing a constant $\Delta t_{\mathrm{cpl}} = 5$ s worked well for this smooth variation, where the coupling is weak and the temporal accuracy of the solution depends mainly on how the imposed temperature change is discretized. When applying the method to industrial cases with a stronger coupling and thermally-induced flow field changes, an automatically adjustable coupling interval is desirable. Sun et al. (2010), for instance, controlled the coupling step size by a deviation of two different temperature history reconstructions, while its accuracy was based on experience. A universally valid indicator is challenging to find, though. The transient FEA is computationally expensive, requiring 83.3 % of the total runtime of 38.1 hours on 28 cores, leaving 15.3 % for the steady frozen CFD with 500 solver iterations each and 1.4 % for the coupling process. Even though there might be potential for optimization such as automatic time stepping, we need to consider that the large number of 151 separate FE and CFD calculations has been necessary to reproduce the transient behavior from $t = 0$ s to $t = 50$ s correctly. Solving the full set of equations increased the computational time of the steady CFD by a factor of 3.8.

CONCLUSIONS

Steady and transient conjugate heat transfer was investigated using a finite element code in the solid and a finite volume computational fluid dynamics program in the fluid domain. The coupling of both codes was realized by a Python-based environment developed in-house. We performed a detailed study on various coupling parameters and how they directly affect the solution with regard to accuracy and convergence behavior.

A combination of Dirichlet and Robin conditions to exchange data at the interface was applied. Two different options to determine the coupling coefficients and the reference temperatures for the solid-side Robin condition were compared. The results suggest that using a global coefficient as relaxation leads to better convergence and more accurate results than using an approach where the coefficient and the reference temperature are calculated based on values at a constant near-wall distance. While a lower stability limit of the global coupling coefficient was identified, choosing the coefficient too large results in slow convergence.

A coupled steady state as well as a transient temperature variation were examined. While temporal accuracy is irrelevant for the steady state coupling, an accurate transient modeling requires subiterations in order to ensure convergence at each coupling step. Provided that the coupling settings are appropriately chosen, good agreement with conjugate reference calculations was observed. The influence of a frozen field approach where only the energy equation is solved was found to be small in the considered case. Findings obtained from the two-dimensional

validation case were extended to the complex case of flow around a three-dimensional vortex generator. Challenges regarding interpolation, spatial heat flux variation, and appropriate residuals were reported. Comparison with transient experiments that examined the spatio-temporal surface temperature using infrared thermography revealed good temporal agreement of temperature and wall heat flux despite spatial differences due to the numerical flow modeling.

As far as computational time is concerned, the conventional approach of calculating a heat transfer coefficient based on a separate isothermal fluid calculation and subsequently imposing this coefficient in conjunction with an appropriate reference temperature on a transient solid calculation may be more efficient. Moreover, it is likely to produce similar results in cases that are subject to only minor changes of the flow field. However, the coupling method presented in this study works even if no suitable reference temperature can be defined and if the heat transfer coefficient is considerably affected by the thermal condition. This applies especially to industrial turbomachinery applications, where velocity and temperature differences are considerably larger than in the cases presented in this paper.

ACKNOWLEDGEMENTS

We gratefully acknowledge the financial support provided by the Friedrich und Elisabeth Boysen-Stiftung.

ILLUSTRATIONS

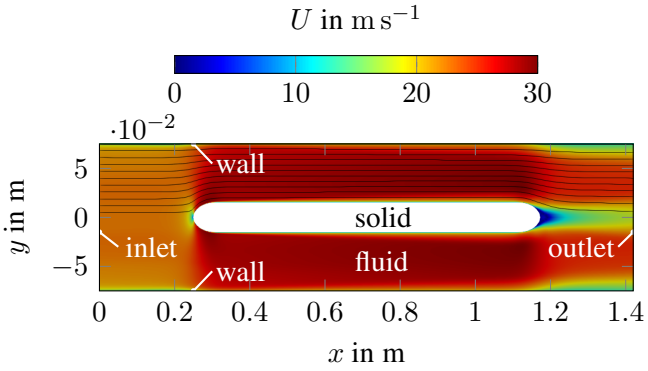

Figure 1: **Computational domain of the channel**

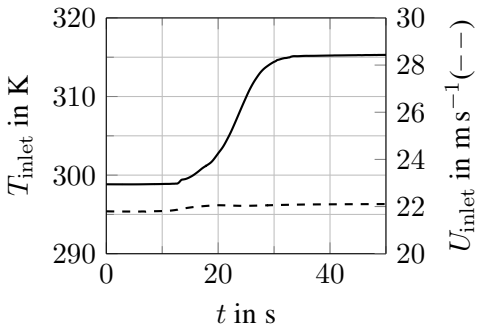

Figure 2: **Variation of inlet temperature**

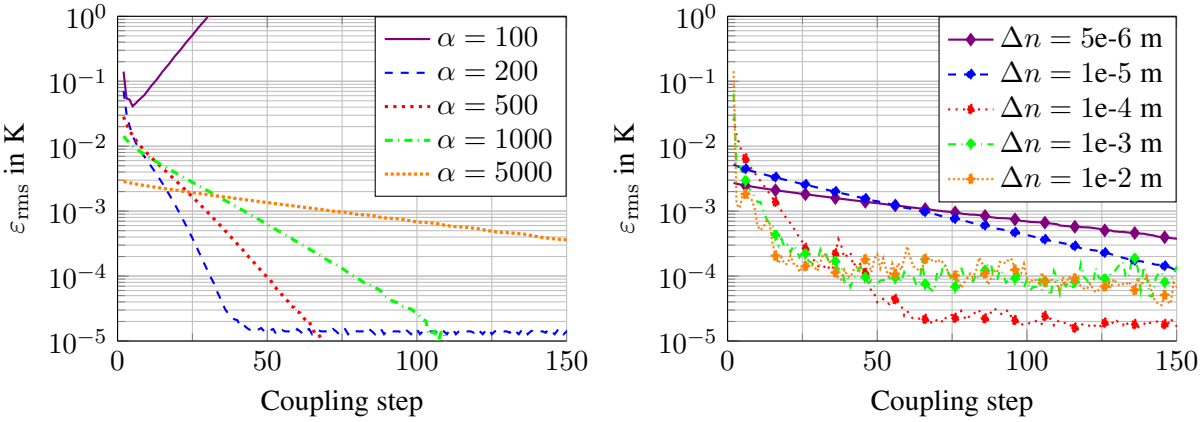

Figure 3: **Convergence behavior of the steady state coupling for different coefficients**

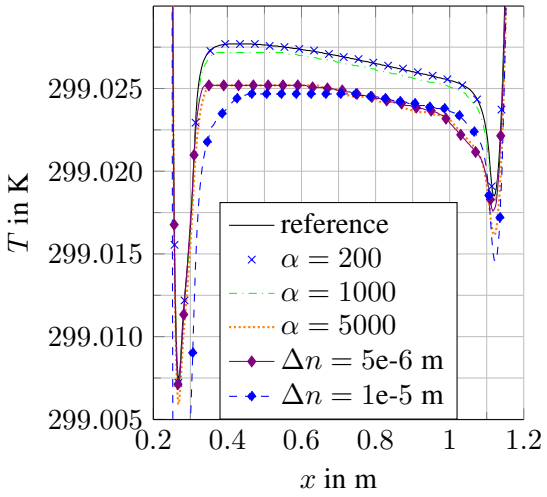

Figure 4: **Steady temperature distribution at the interface**

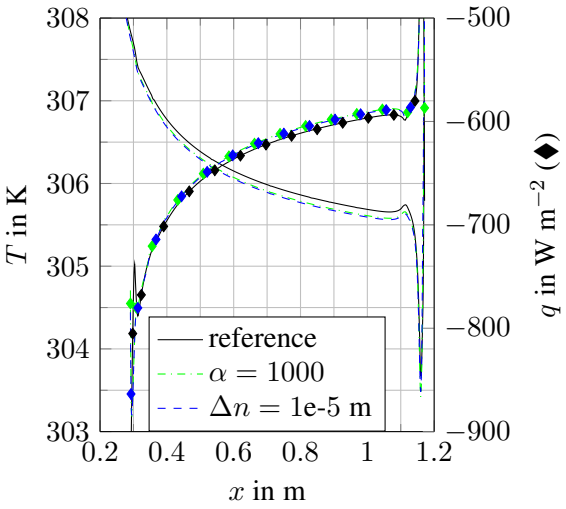

Figure 5: **Temperature and wall heat flux distribution at $\mathrm{t} = 50$ s**

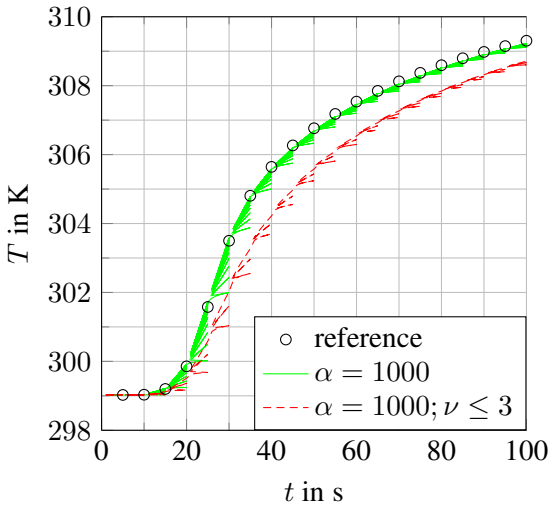

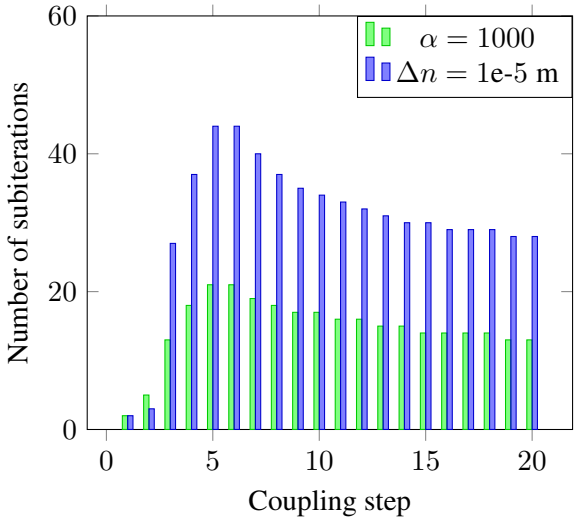

Figure 6: **Temperature evolution on the interface at $\mathrm{x} = 0.402$ m (left) and the corresponding subiterations per coupling step (right)**

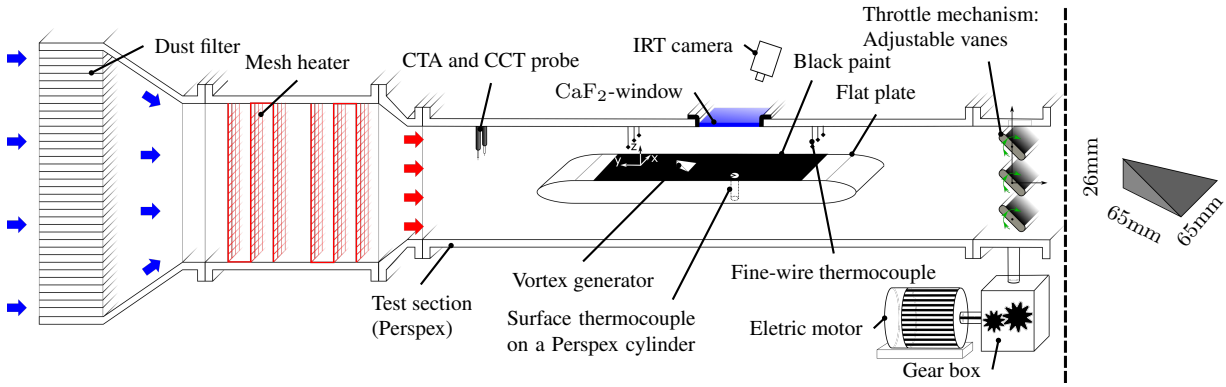

Figure 7: **Experimental setup of the vortex generator test case**

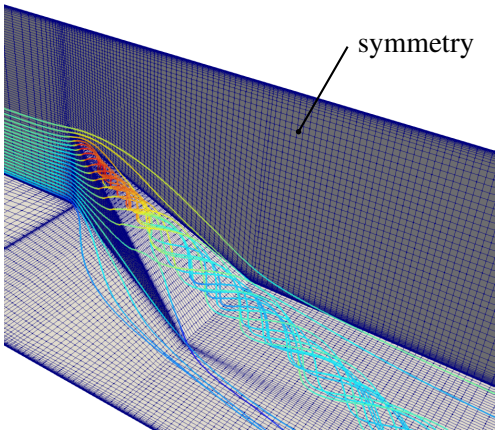

Figure 8: **Section of the computational domain and streamlines around the vortex generator**

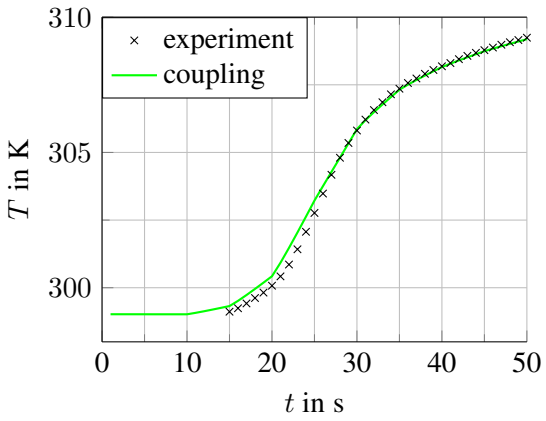

Figure 9: **Temperature evolution at one point on the interface at $\mathrm{x} = 0.541$ m and $\mathrm{z} = 0.037$ m**

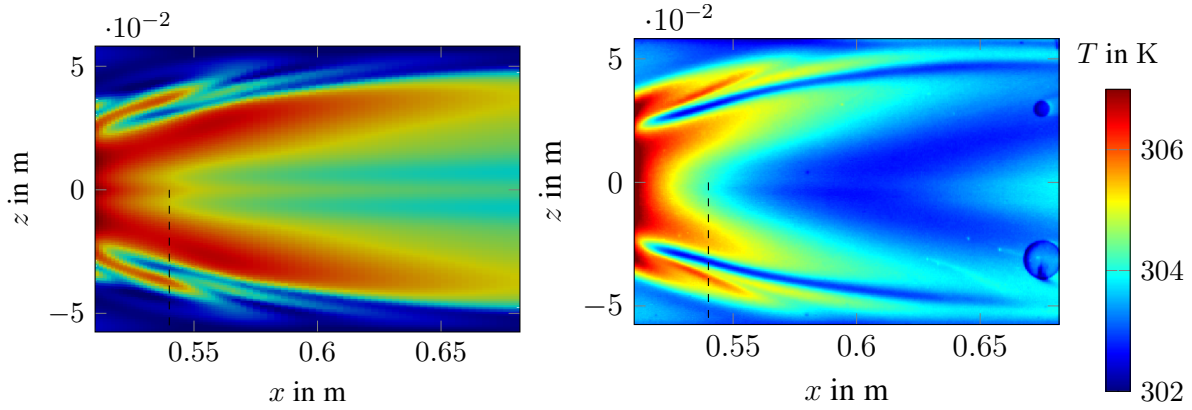

Figure 10: **Numerical (left) and experimental (right) temperature distributions at $\mathrm{t} = 30$ s, dashed line at $\mathrm{x} = 0.54$ m**

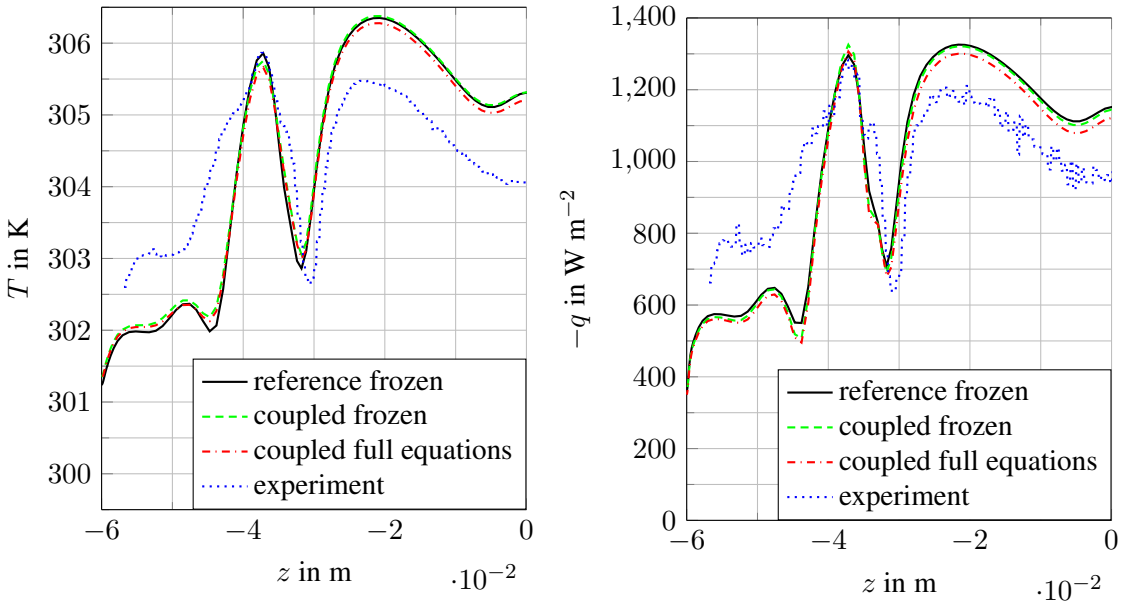

Figure 11: **Temperature (left) and wall heat flux (right) at $\mathrm{x} = 0.54$ m at $\mathrm{t} = 30$ s**

REFERENCES

S. Brack, R. Poser, and J. von Wolfersdorf. Unsteady conjugate heat transfer experiments in the presence of lateral conduction. In *XXIV Biannual Symposium on Measuring Techniques in Turbomachinery*, 2018.

H.-J. Bungartz, F. Lindner, B. Gatzhammer, M. Mehl, K. Scheufele, A. Shukaev, and B. Uekermann. preCICE - a fully parallel library for multi-physics surface coupling. *Computers and Fluids*, 141:250–258, 2016. doi: https://doi.org/10.1016/j.compfluid.2016.04.003. Advances in Fluid-Structure Interaction.

C. Dietz. *Computation of Heat Transfer in Internal Flows with Vortex-Generating Elements*. PhD thesis, University of Stuttgart, 2008.

F. Duchaine, S. Jauré, D. Poitou, E. Quémerais, G. Staffelbach, T. Morel, and L. Gicquel. Analysis of high performance conjugate heat transfer with the openpalm coupler. *Computational Science & Discovery*, 8(1):015003, 2015.

M.-P. Errera and B. Baqué. A quasi-dynamic procedure for coupled thermal simulations. *International Journal for Numerical Methods in Fluids*, 72(11):1183–1206, 2013.

M.-P. Errera, M. Lazareff, J.-D. Garaud, T. Soubrié, C. Douta, and T. Federici. A coupling approach to modeling heat transfer during a full transient flight cycle. *International Journal of Heat and Mass Transfer*, 110:587–605, 2017.

M. Estorf. Image based heating rate calculation from thermographic data considering lateral heat conduction. *International Journal of Heat and Mass Transfer*, 49(15):2545–2556, 2006.

G. Gimenez, M. Errera, D. Baillis, Y. Smith, and F. Pardo. A coupling numerical methodology for weakly transient conjugate heat transfer problems. *International Journal of Heat and Mass Transfer*, 97:975–989, 2016.

M. Henze, J. von Wolfersdorf, B. Weigand, C. F. Dietz, and S. O. Neumann. Flow and heat transfer characteristics behind vortex generators–a benchmark dataset. *International Journal of Heat and Fluid Flow*, 32(1):318–328, 2011.

E. Jones, T. Oliphant, P. Peterson, et al. SciPy: Open source scientific tools for Python, 2001. URL `http://www.scipy.org/`. [Online; accessed 09/15/18].

W. Joppich and M. Kuerschner. MpCCI - a tool for the simulation of coupled applications. *Concurrency and computation - Practice and Experience*, 18(2):183–192, 2006.

Z. Sun, J. W. Chew, N. J. Hills, K. N. Volkov, and C. J. Barnes. Efficient finite element analysis/computational fluid dynamics thermal coupling for engineering applications. *Journal of Turbomachinery*, 132(3):031016, 2010.

Z. Sun, J. W. Chew, N. J. Hills, L. Lewis, and C. Mabilat. Coupled aerothermomechanical simulation for a turbine disk through a full transient cycle. *Journal of Turbomachinery*, 134 (1):011014, 2012.